JOURNAL OF GEOPHYSICAL RESEARCH, VOL. 106, NO. C7, PAGES 14,113–14,128, JULY 15, 2001

Linear transition ripple migration and wave orbital velocity skewness: Observations

Anna M. Crawford[1] and Alex E. Hay

Dalhousie University, Department of Oceanography, Halifax, Nova Scotia, Canada

Abstract. Field observations were made in 3–4 m water depth of linear transition ripple geometry and migration using a high–resolution laser–video bed profiling system and acoustic scanning sensors during both the growth and decay phases of an autumn storm event. Linear transition ripples are long–crested, low–steepness bedforms of the anorbital ripple type and were observed to occur here at relatively high wave energies just below the flatbed threshold, with wavelengths of 8.5 ± 0.5 cm and heights of 0.3 ± 0.1 cm. The maximum observed migration rate was 0.7 cm/min. Migration was offshore during storm growth and onshore during storm decay. The observed ripple migration velocities were highly correlated ($r^2 > 0.7$) with nearbed wave orbital velocity skewness in both cross–shore directions. During storm growth the incident wave spectrum was bimodal and the orbital velocity skewness was negative. During storm decay the wave spectrum was unimodal and the velocity skewness was positive. Bispectral analysis shows that the main contribution to negative velocity skewness during storm growth was due to a difference interaction between the two principal (sea and swell) components of the bimodal velocity spectrum. Positive skewness during storm decay was due to self–self interaction of the narrowband residual swell. The negative velocity skewness observed during storm growth is consistent with prediction by a two–frequency second–order wave theory.

1. Introduction

An understanding of cross–shore sediment transport is central to prediction of many aspects of morphological evolution in the nearshore zone. Generally accepted relationships between characteristics of the fluid forcing and the resulting net sediment transport are lacking, however, especially for the irregular waves typical of field conditions [*Kraus and Horikawa*, 1990].

It has long been thought that wave orbital velocity skewness is fundamentally important to the direction and magnitude of net sediment transport. This idea has physical basis in the difference between the duration and magnitude of the maximum velocities during the forward and reverse flow phases under skewed waves and the nonlinear dependence of sediment transport on fluid velocity. Net movement of sediment under oscillatory flow requires a difference between the transport during the opposing flow phases. The third moment of the velocity (unnormalized skewness) appears in widely used bedload transport models based either on energetics arguments or bottom stress [*Meyer-Peter and Müller*, 1948; *Bailard and Inman*, 1981; *Bagnold*, 1963]. Though these approaches represent a large fraction of the modeling effort, velocity exponents ranging between 3 and 7 can be found in the literature [*Dyer and Soulsby*, 1988; *Sleath*, 1995]. There are very few reported field observations of a direct link between higher–order moments of the nearbed orbital velocity, including skewness, and local sediment transport rate.

Nonzero orbital velocity skewness can result from nonlinear interactions among the frequency constituents of the wave field. For monochromatic waves, self–self interaction leads to the development of the first harmonic, as in the well–known Stokes expansion, and to positive velocity skewness. If a spectrum of waves is present, sum and difference frequency interactions are possible, and the resulting velocity skewness can be negative. *Elgar and Guza* [1985a] show observations of narrow– and broad–banded shoaling waves demonstrating a range of nonlinear interactions contributing to evolution of the skewness and asymmetry of waves propagating into shallower water. These results were presented as bispectra. The bispectrum has been widely used in the study of nearshore wave dynamics [e.g., *Doering and Bowen*, 1995; *Herbers et al.*, 1992; *Norheim et al.*, 1998] since its introduction in that context by *Hasselman et al.* [1963].

[1]Now at: Defence Research Establishment Atlantic, Dartmouth, Nova Scotia, Canada

Paper number 2000JC000612.
0148-0227/01/2000JC000612$09.00

In the past, observations of the relationships between the wave forcing and seabed response have been hampered by practical difficulties associated with the harsh and variable environment. Recent advances in instrumentation are contributing to progress in this area. The purpose of this paper is to present field observations of cross–shore ripple migration and nearbed velocities acquired using a suite of these new sensors. These observations show onshore and offshore migration of linear transition ripples at velocities that correlate with the skewness of the orbital velocity.

Linear transition ripples are low–relief, two–dimensional bedforms which exist in relatively high energy flow, just below the flatbed threshold [*Dingler and Inman*, 1977]. These bedforms are of interest as they occur under conditions when sediment transport rates are likely to be large. As small–scale bedforms, they respond quickly to changes in the forcing. In addition, the two–dimensional geometry ensures that complications to the overlying flow associated with three–dimensionality of the bed are not present. Furthermore, in the results to be presented, the occurrence of this particular bedform type during both the growth and decay phases of a storm event provides an opportunity to investigate the directional response of the bed to differences in the higher–order moments of the wave forcing, at roughly the same wave energy.

The observations of linear transition ripple geometry and migration velocity, determined using both acoustic and laser–video techniques are presented. This is followed by presentation of the orbital velocity measurements. Bispectral analysis is used to relate the orbital velocity spectra to the observed velocity skewness, which correlates with the ripple migration velocity. Nearbed orbital velocity skewness predicted by linear and second–order theories is also compared with the observations.

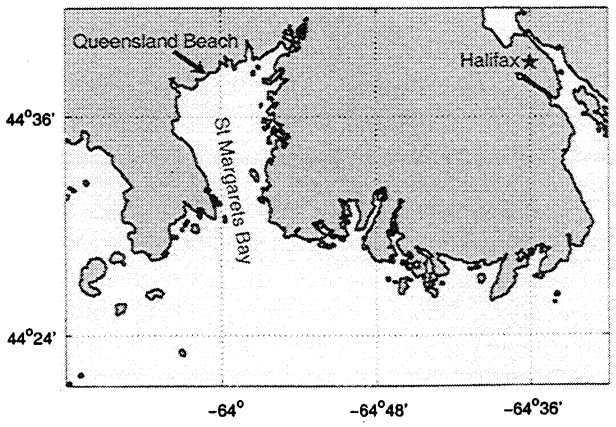

Figure 1. Map of the Nova Scotia coastline west of Halifax showing the location of the field site at the head of St. Margarets Bay.

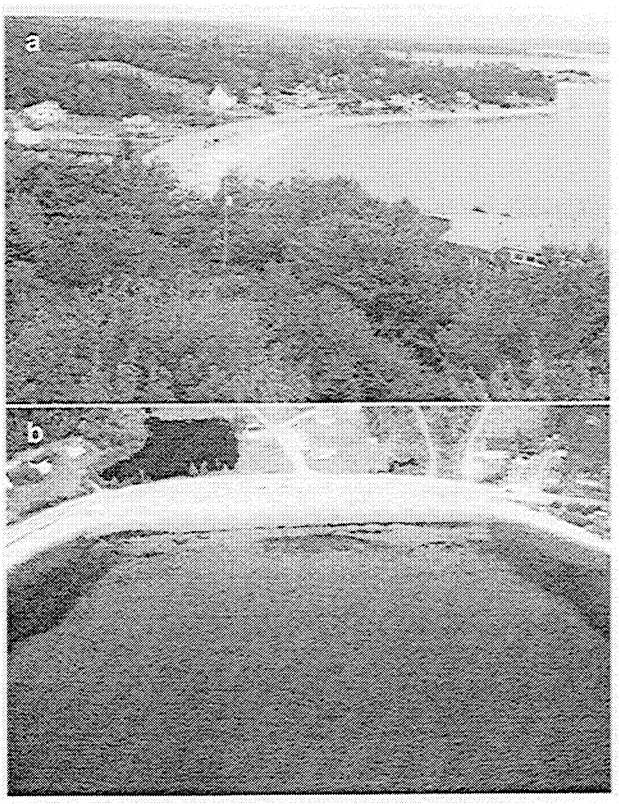

Figure 2. Aerial photos of the experiment site at Queensland Beach, Nova Scotia, looking eastward in Figure 2a and from above in Figure 2b. Both show the pocket beach contained between headlands. (Photos courtesy of A. J. Bowen.)

2. Field Site and Instrumentation

In the autumn of 1995 a joint field experiment was undertaken at Queensland Beach, Nova Scotia, involving Dalhousie University and Memorial University of Newfoundland. This was also the site of a previous collaborative field experiment in 1987 [*Vincent et al.*, 1991]. Queensland Beach is a pocket beach between rocky headlands and is oriented almost normal to wave energy coming in through the narrow mouth of St. Margarets Bay, shown in Figure 1. Aerial photos overlooking the experiment site are shown in Figure 2.

The beach profile (average of three surveys) near the end of the 10 day deployment is shown in Figure 3. The instrument frame was located 60 m offshore of the mean water line, at a mean water depth of 3.2 m, with maximum and minimum depths of 4.1 and 2.4 m during the experiment. The beach slope at that location was ~2°. Samples of the quartz sand collected at the site had a sieved median diameter D_{50} of 174 μm (with $D_{16} = 124$ μm and $D_{84} = 321$ μm).

The deployment configuration is shown in side and plan views in Figure 4. The instruments were mounted on a 3 m section of antenna mast which was cantilevered offshore from a frame (not shown in Figure 4). The

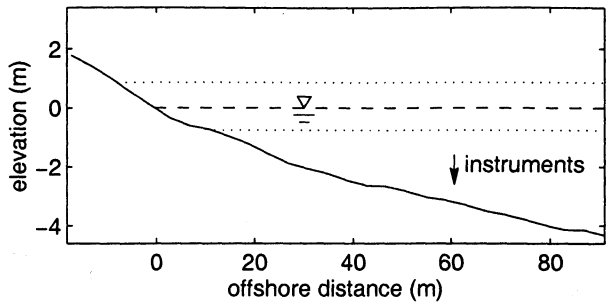

Figure 3. Mean beach profile at the time of deployment at Queensland Beach, Nova Scotia, in the fall of 1995. The dashed line shows the mean water level, and the dotted lines show the highest and lowest tides during the 10 day experiment.

frame was supported by four pipes jetted into the bed, spaced 2 m in the longshore direction and 1.5 m cross-shore. The local bedform field was monitored to a radius of 5 m using a rotary sidescan (fanbeam) acoustic system [*Hay and Wilson*, 1994]. A rotary pencil-beam acoustic system operated at a fixed slant angle 10° below horizontal in the offshore direction and vertically upward (to measure sea surface elevation) with centimeter radial resolution [*Hay and Bowen*, 2001]. A laser-video bed profile imaging system gave 0.75 m long cross-shore bedform profiles with millimeter resolution [*Crawford and Hay*, 1998]. Flow measurements were made with a dual-beam coherent Doppler profiling system (CDP) [*Zedel and Hay*, 1998; *Hay et al.*, 1999]. The acoustic systems operated on a half hour duty cycle (8 min per cycle), with two CDP runs per half hour, and the laser-video system recorded continuously during nighttime hours, though there were power interruptions resulting in a few short gaps in the data stream.

The centers of the acoustic and laser-video bedform profiles were separated in the cross-shore direction by ~3 m and in the longshore direction by ~20 cm. The nearbed velocities were taken from the CDP profiles at a height of 20 cm above the bed, outside the wave bottom boundary layer. The vertically oriented CDP unit was located at the offshore end of the laser-video profiles (see Figure 4), with an ~20 cm alongshore separation. In following discussion, the nearbed wave orbital velocity refers to the demeaned CDP measured horizontal velocity at this height.

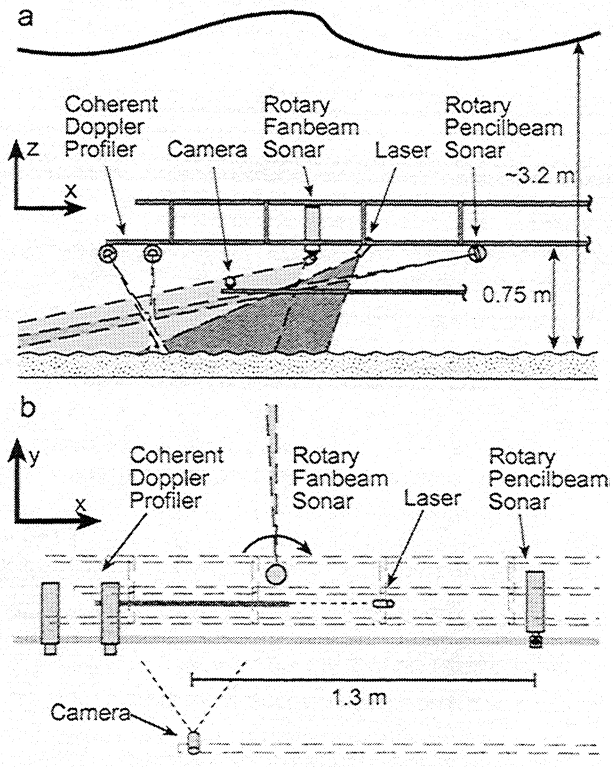

Figure 4. (a) Side view and (b) plan view of the instrument array configuration. In Figure 4b, the laser-illuminated line on the bed is shown by a dark gray band, and the frame outline is dashed. The camera and laser comprise the laser-video system. Beach coordinates are shown with x positive onshore and z positive upward.

3. Autumn Storm Event

A summary of the storm history is given in Figure 5. The storm waves gained amplitude starting early in the

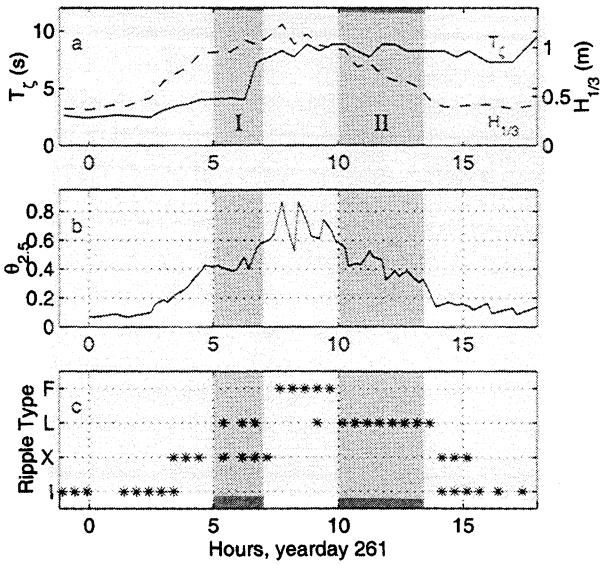

Figure 5. Time evolution of the storm event on yearday 261 in 1995. (a) The period of the peak surface elevation spectra T_ζ (solid) and significant wave height $H_{1/3}$ (dashed); (b) the dimensionless shear stress (grain roughness Shields parameter); (c) the ripple type present as observed from the fanbeam sonar images: I, irregular; X, cross; L, linear transition; F, flatbed. The two time periods to be discussed are shaded gray and labelled intervals I and II.

day, peaking in significant wave height at ~0800 UT and subsiding by 1800 UT. Figure 5a shows the significant wave height $H_{1/3}$ and peak wave period T_ζ. Both were calculated from the surface elevation ζ measured by the upward-looking pencilbeam sonar: the significant wave height is 4 times the standard deviation of ζ [*Thornton and Guza*, 1983], and T_ζ are the surface elevation spectra peak periods. Figure 5b shows the dimensionless shear stress (grain roughness Shields parameter), given by

$$\theta_{2.5} = \frac{1}{2} f_w \frac{(a_o\omega)^2}{(s-1)gD_{50}}, \quad (1)$$

where

$$f_w = \exp\left(5.213\left[\frac{2.5D_{50}}{a_o}\right]^{0.194} - 5.977\right), \quad (2)$$

D_{50} is the median grain diameter, $a_o = 2u_{\rm rms}/\omega$ is the significant orbital semiexcursion, $\omega = 2\pi/T_p$ is the wave radian frequency, T_p is the wave orbital velocity spectrum peak period, s is the sediment specific gravity (2.65 for quartz), and g is acceleration due to gravity. Here f_w is the wave friction factor for turbulent oscillatory flow over a flat bed of fixed grains [*Nielsen*, 1981]. T_p and $u_{\rm rms}$ were determined from the wave orbital velocity u measured by the CDP at a height of 20 cm above the bed. Figure 5c shows the time history of the ripple types that were present in the local area as observed from the half hourly fanbeam sonar images [*Hay et al.*, 1999]. The ripple types have been categorized as "I" for irregular, "X" for cross, "L" for linear transition, and "F" for flatbed.

During the growth of the storm, significant wave height increased, accompanied by a shift to longer peak wave periods, and evolution of bedform type from irregular through cross and linear transition ripples to flatbed when wave height was maximal. As the storm subsided, wave height lessened, and bedform type evolved through linear transition and cross ripples, back to irregular ripples. The time series of ripple type shows that two forms of ripples were often present at the same time and there was a lag in the progression of ripple type relative to the forcing, which has also been observed elsewhere by *Hay and Wilson* [1994].

The two time periods when linear transition ripples were present are shaded gray in Figure 5 and have been labeled intervals I and II for convenient reference. During both intervals, the Shields parameter was between 0.3 and 0.6. Interval I falls during the growth phase of the storm event in the period before flatbed, and interval II is during storm decay after flatbed. Two instances where linear transition ripples have been identified but are not included in intervals I or II were while the waves were near peak height and near the end of the storm at low Shields parameter when the ripples were considered to be relict.

The beach face was surveyed daily from yeardays 254 to 268, except yearday 260, with longer profiles surveyed to beyond the instrument frame on yeardays 254, 264, 265, and 268. The survey on yearday 261 was carried out in the afternoon, after the storm had abated (Figure 5). The difference between this survey and that on yearday 259 shows erosion of the beach face, with an ~5 m retreat of the mean water line. Surveys on the following 3 days show a return to the original configuration by yearday 264. Cusp features were present on yearday 259, eradicated on yearday 261, and reappeared over the subsequent 2 days.

Table 1. Wave Breaking Observations From Upward-Looking Pencilbeam Sonar

Time	h	T_ζ	$H_{1/3}$	H_b	A_b	Observed %
			Interval I			
0545	3.8	4.1	0.96	1.1	3	8
0615	3.9	3.9	1.0	1.1	3	11
0645	3.8	7.3	1.0	1.4	4	13
			Interval II			
1015	3.4	8.9	0.97	1.2	5	23
1045	3.2	8.3	0.80	1.1	3	0
1115	3.1	7.7	0.84	1.2	4	0
1145	3.1	8.9	0.73	1.1	2	0
1215	3.0	8.9	0.66	1.0	2	0
1245	2.9	8.3	0.65	0.9	2	0
1315	2.9	8.3	0.59	0.8	1	1

Time is listed as UT, h is water depth (m), and T_ζ is the peak period of the surface elevation spectra (s). H_b, breaking wave height (m), was calculated from $H_{1/3}$ (m), and A_b is the predicted percentage of waves breaking.

The percentage of waves breaking, determined from bubble plumes in the 8 min upward-looking pencilbeam records, is listed in Table 1 along with the water depth h, peak surface elevation spectral period T_ζ, and significant wave height $H_{1/3}$. For comparison, the predicted percentage of waves breaking A_b was calculated using the relationship $A_b = (H_{\rm rms}/\gamma h)^4$ [*Thornton and Guza*, 1983], where γ is 0.44 and $H_{\rm rms} = H_{1/3}/\sqrt{2}$ [*Thornton and Guza*, 1989]. Also shown is the wave breaking height H_b, calculated from $0.56H_o(L_o/H_o)^{0.2}$, where $L_o = gT_\zeta^2/2\pi$ and H_o are the deepwater wavelength and significant wave height [*Nielsen*, 1992].

To interpret the values presented in Table 1, consider that if the significant wave height $H_{1/3}$ was equal to the wave breaking height H_b then the percentage of waves observed to be breaking should be ~33%. The observed percentage of waves breaking was always less than this value, consistent with $H_{1/3}$ being consistently less than H_b. During interval I, some wave breaking was observed (~10%). Analysis to be presented in Section 6 shows that during interval I the wave spectra were bimodal with short-period sea and longer-period swell peaks. In this case, significant wave height calculated from surface elevation variance is ill defined. Some breaking may

have been due to whitecapping rather than water depth limitation. During interval II, with the exception of the 1015 UT run, no waves were breaking. The upward-looking pencil beam record at 1015 UT contains a few very large breaking events which injected bubbles deep into the water column, persisting for many wave periods and making identification of subsequent breaking events uncertain. The predicted percentage A_b does not compare well with the observations, being low during interval I and high during interval II. This is consistent with the similar poor comparison between A_b and observed wave breaking reported by *Lippmann et al.* [1996]. The observed overall low percentage of waves breaking, however, shows that the measurement area was outside the surf zone, so that wave breaking is not a primary consideration in the results to be presented.

4. Linear Transition Ripple Geometry

In general, the progression from an undisturbed, or relict, bed to flatbed with increasing wave orbital diameter has been described as proceeding from rolling grain ripples just above the critical shear stress for initiation of sediment motion, through vortex ripples (orbital then anorbital) which decrease in steepness quickly as the second critical shear stress leading to flatbed is approached. By virtue of their low steepness, transition ripples have sometimes been included in the category of rolling grain ripples owing to the similar lack of lee vortex formation in both the small and large orbital diameter cases [*Allen*, 1979; *Sleath*, 1976]. The ambiguity of calling the bedforms associated with both low and high sediment transport conditions "rolling grain" ripples is avoided here by referring to the large orbital diameter case as "transition" ripples, following *Dingler and Inman* [1977]. In the past, they have also been called post-vortex ripples [*Clifton and Dingler*, 1984]. *Conley and Inman* [1992] reported transition ripples that were "ephemeral" in nature and were observed reforming during each wave cycle (*Wilson and Hay* [1995] identify "evanescent" ripples which also match this description). The transition ripples reported here persisted through many wave cycles.

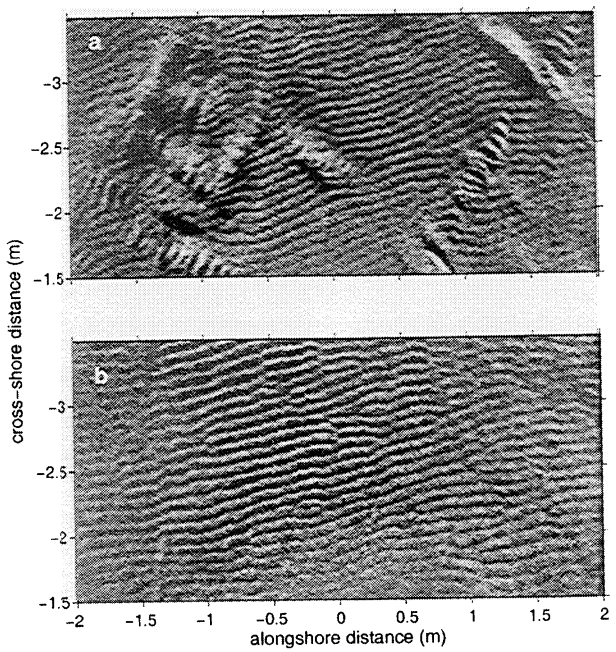

Figure 6. Fanbeam scanning sonar images collected (a) at 0610 UT during interval I, and (b) 1110 UT during interval II. Distance is measured along the bed from the instrument with offshore toward the top of the images.

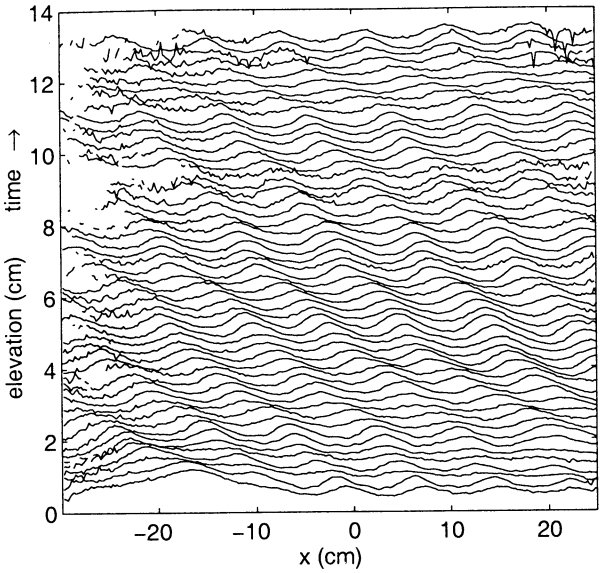

Figure 7. One and a half hour time series of bed elevation profiles obtained using the laser-video system during interval I, starting at 0500 UT. Every fifth profile from the time series shown in Plate 1 is plotted, offset by 0.25 cm each, with time progressing toward the top and offshore to the left.

Figure 6 shows samples from two fanbeam sonar images collected at 610 and 1110 UT, during intervals I and II, respectively. Each is a plan view of the bedform field in a 4 m × 2 m area. Linear transition ripples appear in both images as ~10 cm wavelength, long-crested features. The upper image, from interval I, shows linear transition ripples coexisting with larger cross ripples (see Figure 5). It is possible to follow a single ripple crest across the entire 4 m extent of the lower image, though bifurcations are present. The orientation of the transition ripple crests is inclined at ~15° from the y axis of the instrument coordinate system. These example images show that the ripple wavelength and crest length were similar during both the growth and decay phases of the storm.

The laser-video system gave millimeter resolution profiles of the bedforms along a cross-shore line near the center of the fanbeam field of view (the relative position of the instruments is shown in Figure 4). Time of day and visibility were conducive for laser-video mea-

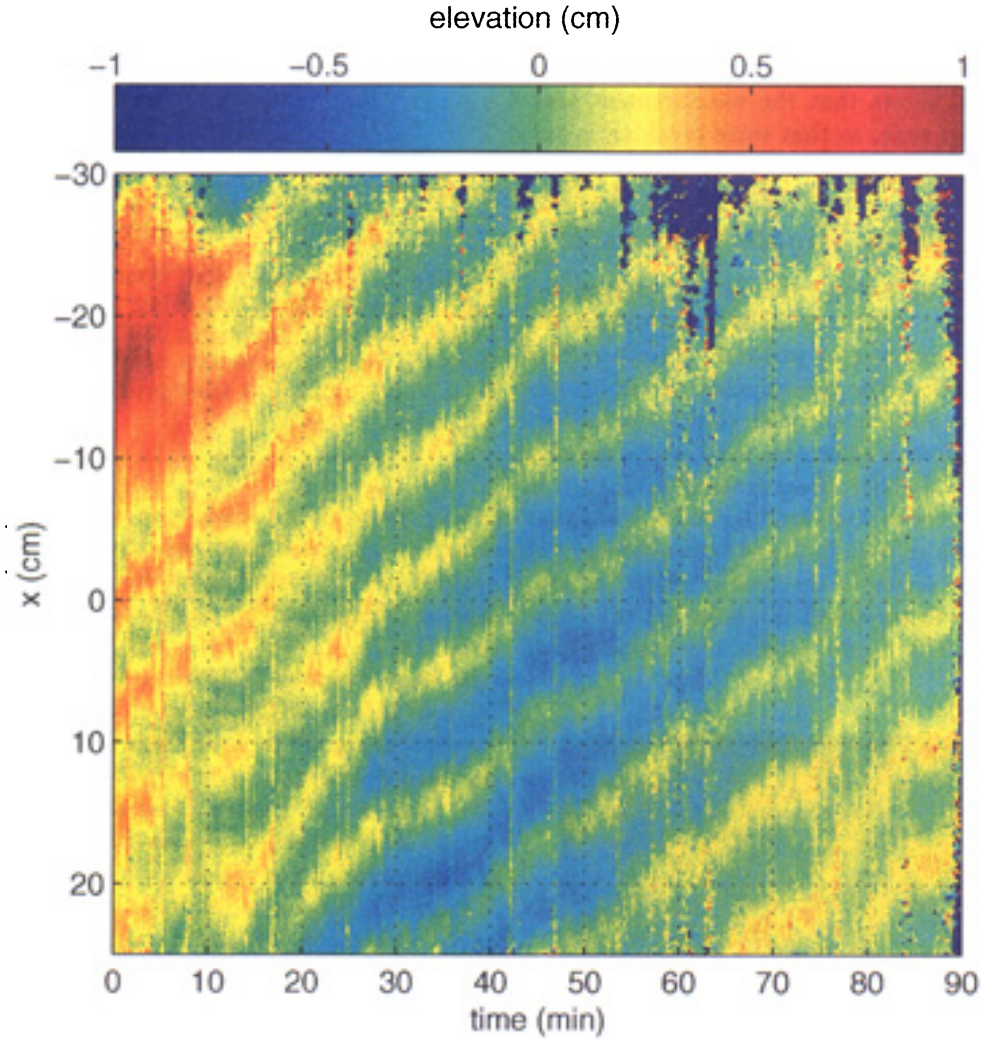

Plate 1. One and a half hour time series of bed elevation profiles obtained using the laser–video system during interval I, starting at 0500 UT. The color scale denotes elevation, and offshore is toward the top. The laser–video origin is located ~25 cm seaward of the fanbeam sonar origin.

surements during the rising stage of the storm event in interval I until sediment in suspension obscured the bed. During interval II, daylight overwhelmed the laser light reflected from the bed despite the use of appropriate filters.

Plate 1 and Figure 7 show a time series of bed profiles over a 90 min period, 0500–0630 UT during interval I. The resolution is ~1 mm in both horizontal and vertical dimensions [*Crawford and Hay*, 1998]. Each profile (vertical line) in the image is an average of 40 profiles collected at 2 Hz. The mean bed slope of ~2° has been removed. Dropouts in the laser–video data (shown in blue) are due to the laser light reflection from the bed being obscured by material in suspension. This happened more frequently at the edges of the laser beam pattern where the light intensity was lower. The laser–video system was much more sensitive to turbidity than the acoustic sensors. At the end of this time series, the light signal from the bed was obscured entirely.

The linear transition ripples shown in the profiles in Plate 1 migrated offshore throughout the duration of this series. These ripples were not "ephemeral"; in fact, the bedform coming into view at the beginning of the series persists for the entire record, long enough to migrate across the entire field of view. This is confirmed by the raw video footage, which shows the largest waves driving sheet flow, which follows the low relief without planing off the ripple crests.

Detailed analysis of the geometry of these bedforms is made possible by the high spatial resolution of the laser–video bed profiles. Figure 8 shows the time evolution of the ripple wavelength λ_r, height η_r, skewness S_r, and asymmetry A_r through the 1.5 hours shown in Plate 1. The center 40 cm of each averaged profile was interpolated onto a regularly spaced horizontal axis (profiles containing dropouts in this region were not included). Wavelength was found from the spatial lag corresponding to the first nonzero positive autocorrelation peak, and height was found from $2\sqrt{2}$ times the root mean square bed elevation (assuming the bedforms are roughly sinusoidal). Ripple profile skewness and asymmetry (using the Hilbert transform method [*Elgar and Guza*, 1985a]) were also calculated from the interpolated profiles. The time series of ripple statistics were broken into 8 min time segments and averaged.

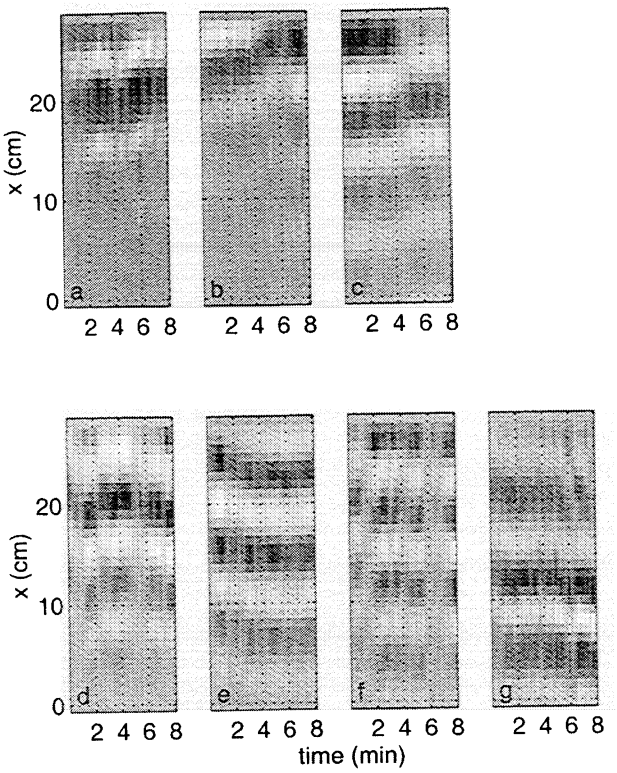

Figure 9. Several 8 min samples of slant pencilbeam acoustic data starting at (a—c) 0510, 0555, and 0625 UT during the growth phase of the storm (interval I) and (d—g) 1125, 1155, 1225 and 1255 UT toward the end of the decay of the storm (interval II). Offshore is toward the top of the images. The 22 min gap between pencilbeam runs makes the identification of particular ripple crests in successive images uncertain.

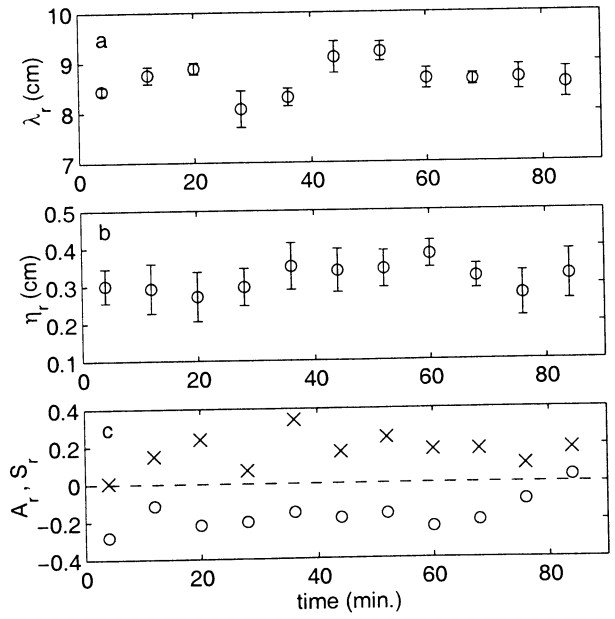

Figure 8. Ripple geometry over 1.5 hours during interval I: (a) wavelength λ_r, (b) height η_r, and (c) bedform profile skewness S_r (crosses) and asymmetry A_r (circles). Each point represents an 8 min average and errorbars show plus or minus one standard deviation.

The variations in ripple wavelength and height over the 1.5 hour period were small, with a mean wavelength of 8.5 cm and height of 3 mm, giving a mean steepness η_r/λ_r of 0.04. These dimensions compare well with those of the transition ripples observed by *Dingler* [1974, Tables 1 and B2] which had heights between 3 and 5 mm and wavelengths between 7 and 8 cm (steepness between 0.04 and 0.07) for smaller-diameter sand (D_{50} of 130—170 μm). *Nielsen* [1981] found $\eta_r/\lambda_r = 0.342 - 0.34\sqrt[4]{\theta_{2.5}}$ for field conditions, which for a Shields parameter of 0.4, predicts η_r/λ_r

= 0.07, higher than for these bedforms, though they lie within the scatter of the observations upon which Nielsen's empirical relation was based [*Nielsen*, 1981, Figure 6]. The orbital excursion doubled during the 1.5 hour time series from ~0.5 to ~1 m with little change in ripple geometry. The ripple profile skewness and asymmetry show that the ripples are somewhat peaked in profile (positive S_r) and lean offshore (negative A_r), though the calculated asymmetry of the bedforms is sensitive to the bed slope, which has been removed. *Clifton* [1976] reported observations of ripple asymmetry as a function of $\Delta u_{1/3} = |u^+_{1/3}| - |u^-_{1/3}|$, the difference of the averaged one-third largest velocities during the forward and reverse flows, noting that asymmetric ripples generally migrate and in the direction of the slip faces. The low relief of these transition ripples suggests that the steeper face was not, in fact, a slip face so that the mode of migration would not have been by avalanching; however, they were asymmetric in the direction of migration, nonetheless.

Independent measurements of bedforms were obtained using the pencilbeam sonar operating at a fixed slant angle, 10° below horizontal and directed offshore. Each image in Figure 9 is an 8 min time series of acoustic intensity profiles. The acoustic backscatter from the ripple slopes facing the instrument appears as dark bands. The center of the acoustic beampattern intersected the bed ~4.2 m along the bed from the instrument, $(x, y) = (-3.2 \text{ m}, -0.27 \text{ m})$ in fanbeam coordinates (Figure 6), or 2.9 m offshore of the center of the laser-video profiles. Range along the bed is calculated from the instrument height above bottom, correcting for the slant angle and assuming a planar bed with a 2° offshore slope. The raw acoustic data were often saturated in intensity over the center of the beampattern. The profiles shown are taken from the offshore shoulder of the beampattern and have been high-pass filtered to remove the long-wavelength intensity modulation due to the beampattern itself.

The first three images in Figure 9 were recorded during the growth phase of the storm (interval I), and the last four were recorded during storm decay (interval II). It can be seen that ripple migration was offshore during the growth of the storm, consistent with the laser-video data, Plate 1, and onshore during interval II as the storm subsided. The average ripple wavelength calculated from the pencilbeam sonar bed profiles, by the same method as for the laser-video profiles, is 8.5 cm in both intervals I and II. The similarity of ripple wavelength during the two time periods is further confirmed by inspection of the fanbeam sonar images (Figure 6). The ripple profile is only occasionally indistinct in the pencilbeam sonar data (gray vertical bands) when suspended material is of sufficient concentration to obscure the bed. In the case of Figure 9f, the ripples may have been erased by the flow. Both the pencilbeam acoustic and laser-video bed profiles indicate, however, that in general, the ripples persist for much longer than a wave period timescale.

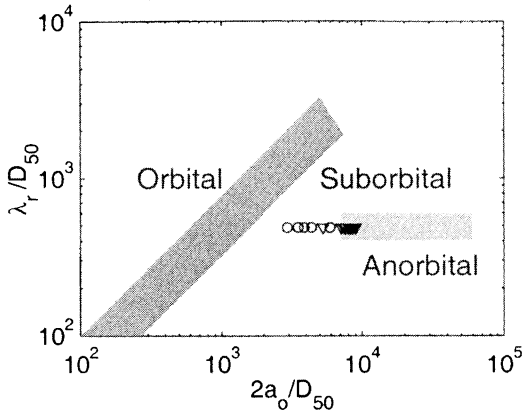

Figure 10. The position of the observed linear transition ripples in orbital diameter–ripple wavelength space, nondimensionalized by median grain diameter, adapted from *Clifton and Dingler* [1984]. Symbols indicate observations from interval I (circles) and from interval II (triangles).

The observed lack of dependence of ripple wavelength on wave orbital diameter and large orbital excursion-to-ripple wavelength ratio (5 to 10) are defining features of anorbital ripples [*Clifton and Dingler*, 1984]. Figure 10 shows a ripple-type classification scheme in terms of ripple wavelength and wave orbital diameter, nondimensionalized by median grain diameter, adapted from *Clifton and Dingler* [1984]. The positions of the observed linear transition ripples in this parameter space are shown by the symbols, using the average ripple wavelength of 8.5 cm, the significant wave orbital diameter calculated from the CDP orbital velocities, and the median grain diameter of 174 μm. The larger orbital diameter cases lie within the anorbital ripple area on the diagram, while the lower orbital diameter cases fall in the suborbital class. *Wiberg and Harris* [1994] found anorbital ripple wavelength to depend on grain diameter as $\lambda_{ano} = 535 D_{50}$. They also found anorbital ripple height to be loosely dependent on wave orbital diameter, such that $\eta_{ano} < 2a_o/100$. For a median grain diameter of 174 μm and orbital diameter of 1 m these criteria yield $\lambda_{ano} \approx 9$ cm and $\eta_{ano} < 1$ cm, consistent with the present ripple observations.

5. Ripple Migration Velocities

The bedform migration velocity was determined from the laser-video profiles during interval I and from the slant pencilbeam acoustic data over the duration of the storm. For both data sets, ripple displacement was calculated by finding the lag of the peak correlation between successive 30 sec mean bed profiles. The laser-video migration velocity time series was broken into 8 min segments for averaging, to match the length of

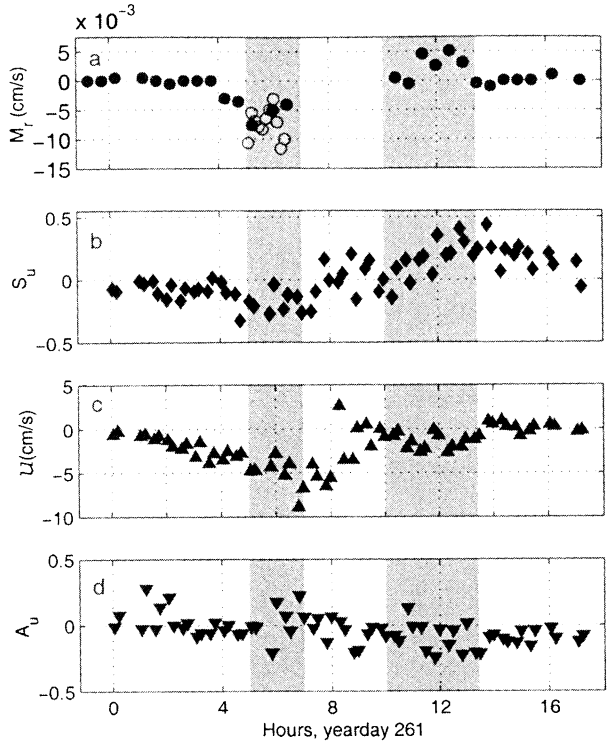

Figure 11. (a) Ripple migration velocity M_r determined from the pencilbeam sonar (solid circles) and laser-video (open circles) data sets, (b) nearbed orbital velocity skewness S_u, (c) mean velocity U, and (d) orbital velocity asymmetry A_u. All are averages over 8 min time series. Intervals I and II are shaded.

the pencilbeam sonar time series. Figure 11d shows the 8 min averaged migration velocities calculated by this method from both data sets along with nearbed orbital velocity skewness S_u, mean velocity U, and asymmetry A_u. Intervals I and II are shaded. There were no migration velocity data for the period between 0700 and 1000 UT owing to the absence of bedforms during flatbed conditions. Between 1000 and 1100 UT, migration of bedforms was switching direction between onshore and offshore over the 8 min runs with net rates close to zero. These low migration rates are distinct from similarly small values at the beginning and end of the storm when the Shields parameter was low and there was no coherent migration of the irregular ripple field.

During interval I, ripple migration was offshore (negative). During interval II, ripple migration reversed to the onshore (positive) direction. The maximum observed offshore migration rate was $\sim$0.012 cm/s (0.7 cm/min), and the maximum onshore rate was $\sim 5 \times 10^{-3}$ cm/s (0.3 cm/min).

Comparison of Figures 11a and 11b shows that the orbital velocity skewness was negative while ripple migration was in the offshore direction and evolved to positive as ripple migration direction reversed to onshore. In fact, the correlation (r^2) between transition ripple migration velocity and orbital velocity skewness during intervals I and II is better than 0.7, as shown in Figure 12. The regression line has a small negative offset in migration velocity for zero skewness. This negative offset is consistent with the small offshore mean nearbed flow velocity during both intervals (see Figure 11c): that is, the mean current would drive offshore migration even for zero orbital velocity skewness. This is discussed further in the Appendix.

Dingler and Inman [1977] found positive correlation between transition ripple migration rate and *Longuet-Higgins'* [1957] nearbottom streaming velocity, $u_s = 5(a_o\omega)^2/4c$, where c is the wave phase speed. Streaming velocity depends on orbital velocity squared, or flow energy, since $a_o\omega \sim 2u_{\rm rms}$. This mechanism predicts ripple migration only in the direction of wave propagation, contrary to what was observed in interval I.

Traykovski et al. [1999] have reported observations of two-dimensional meter wavelength orbital ripples on the open shelf in 12 m water depth and found that ripple displacement correlated with the cumulative integral of $\overline{u^3}$, which was always positive. Figure 12 shows the regression of the ripple migration velocity with the skewness of the nearbed orbital velocity. The correlation with u^3 was as good, as well as with u^5 (both have $r^2 \sim 0.8$). This is not entirely surprising as u^3 and u^5 are themselves correlated with $r^2 > 0.9$. The correlation to higher odd powers of u drops off, and the correlation to $u|u|$ is very low ($r^2 \sim 0.1$).

6. Wave Orbital Velocity Spectra

Figure 13 shows the orbital velocity power spectral density during the two intervals, calculated from the eight 8 min CDP runs during interval I and from ten runs during interval II. The CDP runs were low-pass filtered and resampled at 9.6 Hz (decimated to 4096 from 12000 samples) to roughly match the pencilbeam

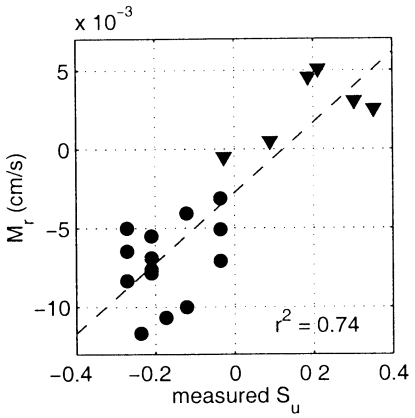

Figure 12. Transition ripple migration velocity M_r plotted against orbital velocity skewness S_u with a linear regression (dashed line). Only migration velocities for linear transition ripples are shown, with circles denoting those occurring during interval I (both acoustic and laser-video measurements) and triangles denoting those occurring during interval II.

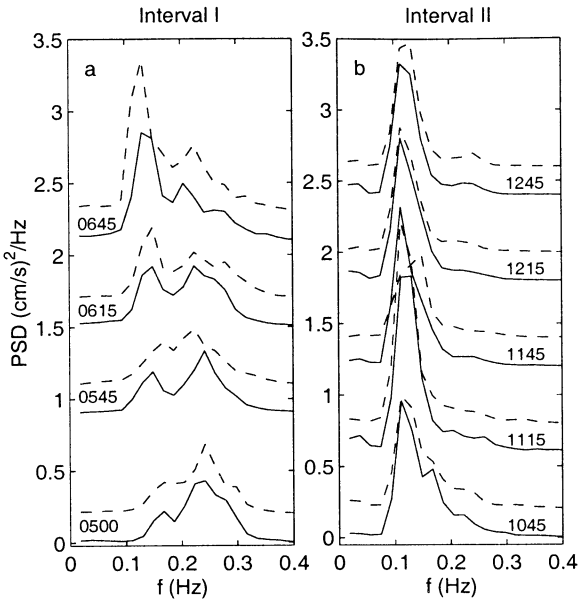

Figure 13. Power spectral densities of CDP measured nearbed orbital velocities during (a) interval I and (b) interval II. The spectra pairs (alternating solid and dashed lines) come from 8 min CDP runs started 10 min apart, labeled with the start time of the first. A vertical offset proportional to the time elapsed from the first run in each interval has been applied.

sample rate of 8 Hz for the skewness calculations. For spectral analysis the CDP records were then broken into 512 sample segments with 75% overlap and windowed with a Hanning window.

During interval II the orbital velocity spectra were unimodal, whereas the spectra during interval I were distinctly bimodal (Figure 13). It is also evident that the spectra remained quasi-stationary through the duration of interval II, whereas there was a progressive strengthening of the lower frequency (swell) peak during interval I. All eight runs from interval I are included in the following analysis despite this apparent lack of stationarity. This was necessary in order to obtain the number of degrees of freedom required for statistical significance of the bispectral results to be presented in Section 7. All the spectra from interval I show bimodality with similar peak frequencies, which will be demonstrated to be a feature of importance to the local dynamics.

Ensemble-averaged spectra for the two intervals are shown in Figure 14, with the peaks relevant to following discussion indicated by arrows and labeled. The spectral density during interval I is bimodal in the incident wave band, with peaks at 0.14 and 0.23 Hz (f_I and f_I'). The interval II spectrum shows a single dominant peak at 0.12 Hz (f_{II}), with a small shoulder at $2f_{II}$. The spectra indicate evolution of the wave forcing through the storm from locally generated short-period seas to longer-period swell.

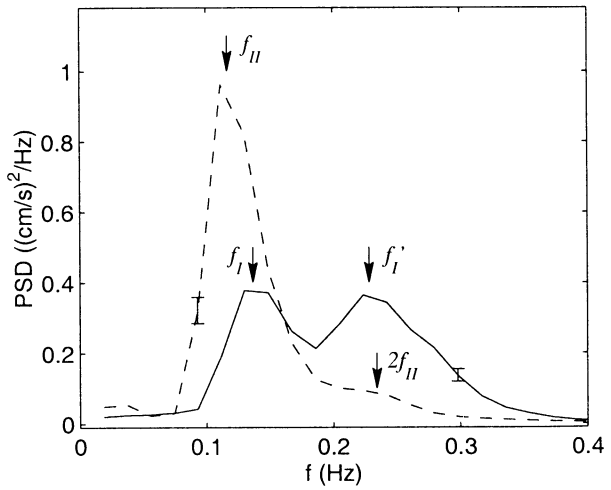

Figure 14. Averaged power spectral densities of nearbed orbital velocity during interval I (solid line) and interval II (dashed line). The 95% confidence limits are shown with each curve (94 degrees of freedom for interval I and 158 for interval II). The spectral peaks are labeled f_I and f_I' for interval I and f_{II} for interval II.

7. Origin of the Orbital Velocity Skewness

In time series of wave quantities (e.g., velocity or surface elevation), nonzero skewness can arise through nonlinear processes, so skewness becomes a measure of nonlinearity. Bispectral analysis is a useful tool for examining time series for weakly nonlinear interactions [*Elgar et al.*, 1995; *Herbers and Guza*, 1994]. Bicoherence can be defined as

$$\beta(f_1, f_2) = \frac{|B(f_1, f_2)|}{(E[|C(f_1)C(f_2)|^2]E[|C(f_1 + f_2)|^2])^{1/2}}, \quad (3)$$

where $B(f_1, f_2) = E[C(f_1)C(f_2)C^*(f_1 + f_2)]$ is the bispectrum, $E[x]$ is the expectation value of x, and $C(f)$ is the complex Fourier coefficient at frequency f [*Elgar*

Table 2. Frequency Pairs Showing Significant Bicoherence for Intervals I and II

Peak	f_1 (Hz)	f_2 (Hz)	β	$\Re\{B\}$
		Interval I		
1	0.23 (f_I')	0.23 (f_I')	0.27	+0.01
2	0.14 (f_I)	0.09 ($f_I' - f_I$)	0.25	−0.06
3	0.23 (f_I')	0.14 (f_I)	0.17	+0.03
		Interval II		
4	0.12 (f_{II})	0.12 (f_{II})	0.38	+0.15
5	0.24 ($2f_{II}$)	0.12 (f_{II})	0.22	0

Bicoherence is labeled β, and the magnitude of the real part of the bispectrum is labeled $\Re\{B\}$.

and Guza, 1985a; *Kim and Powers*, 1979]. Further, a property of the velocity bispectrum is that

$$E[u(t)^3] = \sum_{f_1,f_2} \Re\{B(f_1, f_2)\} , \quad (4)$$

where $\Re\{\ \}$ denotes the real part and $E[u(t)^3]$ is the third moment of the zero mean $u(t)$ time series, related to skewness S by

$$S = \frac{E[u(t)^3]}{E[u(t)^2]^{3/2}} . \quad (5)$$

For the bicoherence normalization used here the 95% significance level for zero bicoherence is given approximately by (6/degrees of freedom)$^{1/2}$ [*Elgar and Guza*, 1988].

Figure 15 shows the orbital velocity bicoherence for the two time intervals, up to 0.4 Hz. The lowest contour level is at the 95% significance level. The frequency resolution, with two-point merging in both frequency dimensions, is 0.037 Hz. Areas of significant bicoherence indicate frequency pairs (f_1, f_2) that are involved in either sum or difference triad interactions (f_1, f_2, $f_1 + f_2$). The frequency locations of the significant bicoherence peaks are summarized in Table 2, with reference to frequencies labeled in Figure 14. Note that the bicoherence frequency resolution is lower than that of the spectral densities so that the bicoherence peak locations may be offset from the spectral density peaks.

Figure 15 also shows the real part of the bispectrum of the orbital velocity for the two intervals. Significant nonzero $\Re\{B\}$ is limited to frequencies below 0.4 Hz. The real part of the bispectrum is related to skewness by (4) and (5). The sign of $\Re\{B\}$ at a location in frequency–frequency space indicates the sign of the skewness arising from the interaction involving those frequencies. The column labelled $\Re\{B\}$ in Table 2 indicates the value of $\Re\{B\}$ at the frequencies of the bicoherence peaks.

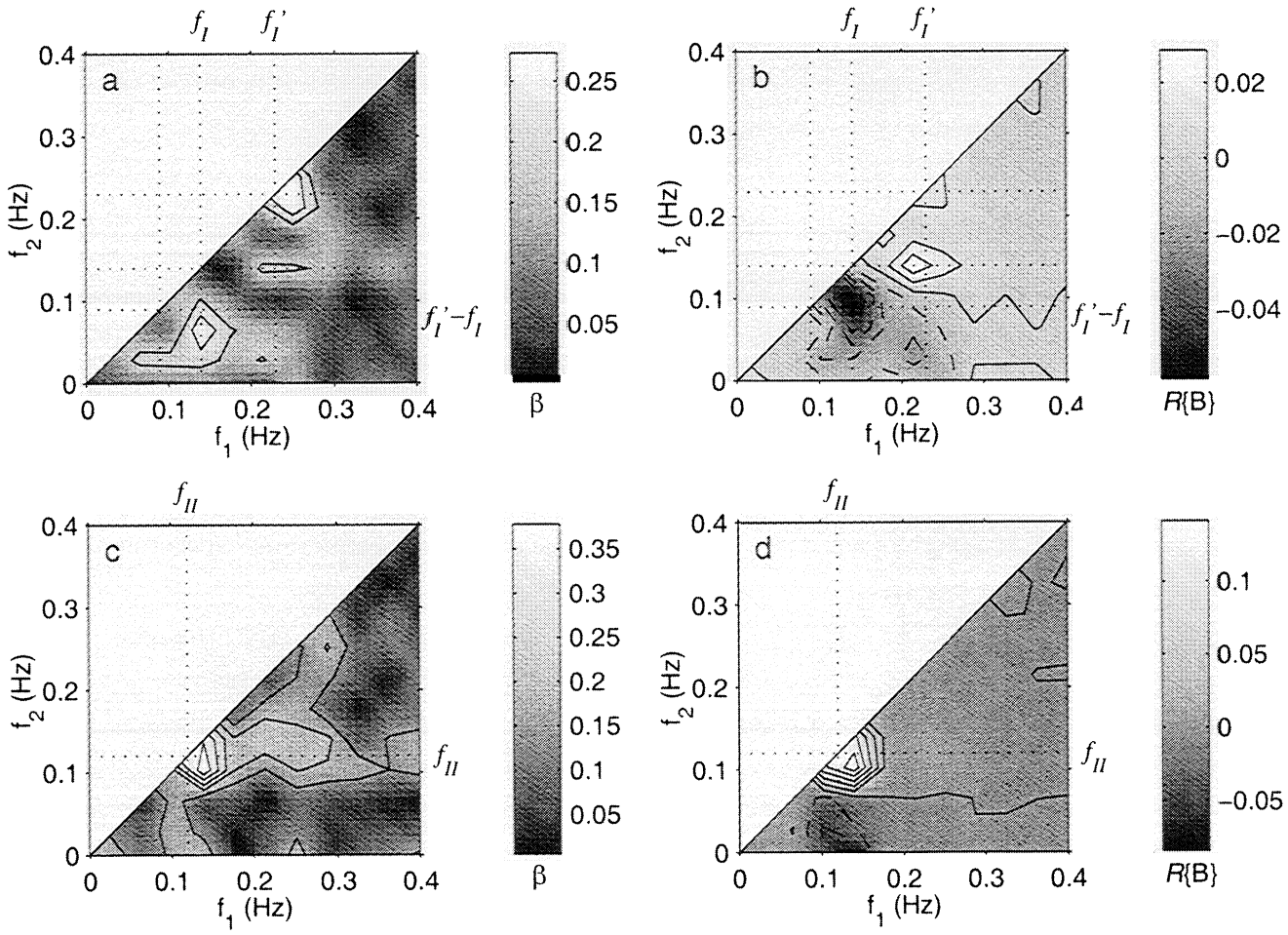

Figure 15. (a and c) Nearbed orbital velocity bicoherence and (b and d) the real part of the bispectrum during (a and b) interval I and (c and d) interval II. The lowest bicoherence contour is at the 95% confidence limit, with 188 degrees of freedom in Figure 15a and 316 in Figure 15c, with successive contours 0.05 apart. The dashed contours of $\Re\{B\}$ are negative values and solid contours are zero and positive, at intervals of 0.002 in Figure 15b and 0.005 in Figure 15d. The gray scales are indicated by the bars. The spectral peak frequencies for both intervals (see Figure 14) are shown by the dotted lines.

During storm growth the bimodal orbital velocity spectrum shows the development of a progressively more energetic lower frequency swell peak. The real part of the bispectrum for interval I (Figure 15b) is negative around peak 2 (Table 2), while peak 1 is a positive self–self interaction peak of lesser magnitude. Peak 3 has positive $\Re\{B\}$ from a sum interaction between frequencies f_I' and f_I but has low bicoherence. The large negative $\Re\{B\}$ peak leads to an overall negative integrated orbital velocity bispectrum (negative skewness). This peak results from a difference interaction between frequencies f_I and f_I', the peak frequencies of the bimodal interval I orbital velocity spectrum: $(f_1, f_2, f_1 + f_2) = (f_I, f_I' - f_I, f_I')$.

During storm decay the dominant peak in the unimodal velocity spectrum is the swell peak which had increased in energy through interval I and evolved to a slightly lower frequency, 0.12 Hz (f_{II}) (see Figure 13b). The real part of the bispectrum and the bicoherence both show strong positive self–self interaction peaks associated with the swell (peak 4, Table 2) but no $\Re\{B\}$ peak at the frequencies of the smaller harmonic bicoherence peak, peak 5. The small negative peak in $\Re\{B\}$ at $(f_1, f_2) = (f_{II}, 0.02$ Hz) has low bicoherence. The orbital velocity skewness in interval II is dominated by the large positive self–self interaction at the swell frequency peak of the orbital velocity spectrum.

8. Comparison With Theory

As a first comparison with theory, nearbed orbital velocity was calculated from surface elevation time series measured by the pencilbeam sonar. Frequency components of the surface elevation spectra were depth attenuated using linear theory and the full dispersion relation; then the velocity was reconstructed by inverse Fourier transform. Figure 16 shows the comparison between the skewness of the surface elevation–derived orbital velocity and of the measured orbital velocity. Though there is a bias toward higher skewness of the computed velocity, the points are scattered close to the 1:1 line. This indicates that the nonlinear contributions to the vertical transformation of the wave orbital velocity are small in this case [*Guza and Thornton*, 1980]. The skewness of the surface elevation itself is also shown and is always larger (and positive), as expected: the high-frequency components of the surface elevation are filtered out by depth attenuation, leading to lower (and sometimes negative) skewness of the calculated orbital velocity.

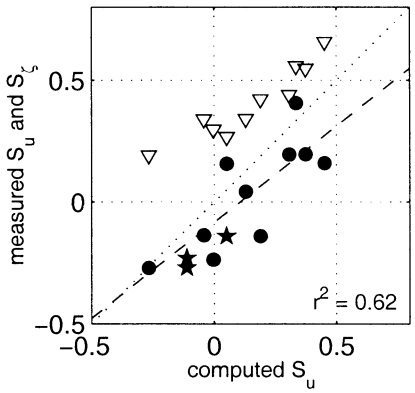

Figure 16. Comparison of measured velocity skewness with that of velocity calculated from surface elevation for both intervals (circles). Comparison with the skewness of velocity calculated from (6), at three times during interval I are also shown (stars). The triangles indicate the skewness of the measured surface elevation S_ζ. The dashed line is a least squares linear regression to the circles (linear velocity calculation comparison).

Table 3. Comparison of the Skewness of CDP Measured Velocity and Velocity Calculated Using (6) at Three Times During Interval I (h = 3.8 m) and the Ursell Numbers.

Time	S_{meas}	S_{calc}	Ur_1 / Ur_2	Ur_{S1} / Ur_{S2}	Ur_{D1} / Ur_{D2}
0545	−0.27	−0.11	0.07 / 0.02	0.10 / 0.08	−0.24 / −0.19
0615	−0.23	−0.11	0.10 / 0.02	0.09 / 0.10	−0.22 / −0.25
0645	−0.14	0.05	0.17 / 0.03	0.13 / 0.20	−0.24 / −0.37

Time is in UT. The Ursell numbers Ur are the ratios of the second-order terms to the first order term for the two wave trains at frequencies f_I, $i = 1$, and f_I', $i = 2$ ($Ur_i = \mathcal{B}_i/\mathcal{A}_i$, $Ur_{Si} = \mathcal{S}_{21}/\mathcal{A}_i$, and $Ur_{Di} = \mathcal{D}_{21}/\mathcal{A}_i$).

A further comparison was made between the skewness of the measured velocity and that of a two-frequency second-order orbital velocity calculated from surface elevation parameters. A representation of orbital velocity including second-order sum and difference interactions for two monochromatic colinear wave trains has been given, among others, by *Biésel* [1952] based on the work of *Miche* [1944], as

$$u = \sum_{i=1}^{2} \{\mathcal{A}_i \cos \omega_i t + \mathcal{B}_i \cos 2\omega_i t\} + \mathcal{S}_{21} \cos[(\omega_2 + \omega_1)t] + \mathcal{D}_{21} \cos[(\omega_2 - \omega_1)t], \quad (6)$$

where $\mathcal{A}_i$ and $\mathcal{B}_i$ are the first- and second-order Stokes coefficients and $\mathcal{S}_{21}$ and $\mathcal{D}_{21}$ are the second-order sum and difference interaction coefficients. The coefficients depend on the water depth and height above bottom and the surface elevation amplitudes, wavenumbers k_i, and frequencies ω_i of the two wave trains, which have been determined here from the measured surface elevation spectra. The resulting orbital velocity, through second-order wave–wave interaction, can have positive

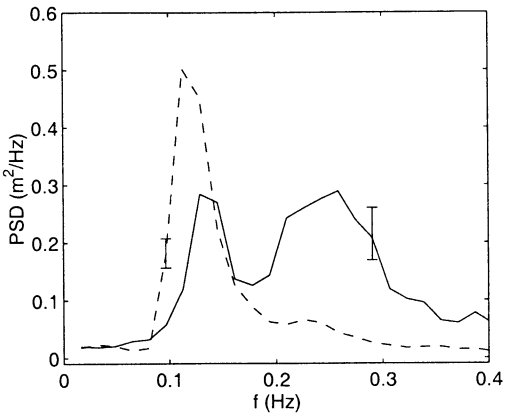

Figure 17. Ensemble–averaged power spectral densities of surface elevation measured using the upward–looking pencilbeam sonar during interval I (solid line) and interval II (dashed line). The 95% confidence limits are shown with each spectrum.

or negative skewness depending on the balance between positive second harmonic $\mathcal{B}_i$ and sum interaction $\mathcal{S}_{21}$ contributions and the negative difference interaction $\mathcal{D}_{21}$ contribution. This two–frequency form for u can be shown to be equivalent to the more general spectral representation given by *Hasselman et al.* [1963] for the case of two colinear monochromatic wave trains [*Crawford*, 2000].

The ensemble–averaged surface elevation power spectral densities for the two time intervals are shown in Figure 17, calculated from pencilbeam sonar time series. During interval I, CDP velocity measurements coincided on three occasions with pencilbeam surface elevation measurements. Taking the frequencies and amplitudes of the two interacting waves from the two peaks of the surface elevation spectra at each of these times, nearbed velocity was calculated using (6). The skewness of the three resulting velocities are shown in Figure 16. As with the linear theory comparison, the calculated velocity skewness has a tendency toward more positive values than the observations, though is quite favorable in general. A similar calculation including the self–self interaction seen during interval II strongly overestimates the observed positive velocity skewness. The ensemble–average of the skewness of the measured velocity during interval II was 0.12, while the ensemble–averaged calculated value was 0.60. Overprediction of the positive contributions to velocity skewness by this type of calculation has also been noted by *Herbers and Burton* [1997] in comparison to Boussinesq theory.

For validity of the second–order perturbation representation of velocity the ratios of the second–order coefficients $\mathcal{B}_i$, $\mathcal{S}_{21}$, and $\mathcal{D}_{21}$ to the first–order coefficient $\mathcal{A}_i$ (the Ursell numbers) must be small. These are listed in Table 3 for the pairs of waves at frequencies f_I and f_I' (i = 1 and 2) at each of the three times during interval I. The larger values of Ur_D show amplification of the difference frequency response in shallow water [*Phillips*, 1960]. The largest value, $Ur_{D2} \sim 0.4$, coincides with the poorest comparison between calculated and measured velocity skewness (in the sense that the predicted sign is incorrect). During interval II the Ursell number is similarly large (the ensemble–averaged $Ur = 0.33$). In these cases, the second–order terms are larger than mere perturbations and outside the range of validity of this approach.

9. Additional Considerations

The effects of nonnormal wave incidence and, potentially of more relevance to wave interaction, directional spread in the incoming wave forcing [*Elgar and Guza*, 1985b; *Herbers and Guza*, 1994] have not been considered in this analysis. Figure 6 clearly shows that the ripple crests were aligned ~15° from the y axis of the measurements, in a direction roughly parallel to the large–scale shoreline of the head of the bay. This means that the measurements of ripple wavelength and migration velocity, shown in Figures 8 and 11, are ~3% larger than the actual crest–normal values. This is a sufficiently small difference that correction has not been made. If it is supposed that the ripple crests were oriented normal to the dominant wave incidence direction, then in this case, the measured horizontal orbital velocity component would be correspondingly smaller by 4% than in a ripple crest–oriented coordinate system. The effect of an unresolved orthogonal velocity component has not been assessed; however, multiplication by a constant factor does not affect the skewness of u. Despite these potential complications the one–dimensional approach which has been taken here appears to provide a reasonable explanation of the observations.

10. Conclusions

Field observations of linear transition ripples (low–relief, long–crested, anorbital bedforms) obtained using the laser–video system are part of a comprehensive data set which also includes high–quality nearbed velocity and scanning sonar bedform measurements. The transition ripples existed in energetic flow conditions, just below the flatbed threshold. This set of observations provides valuable insight into sediment transport processes in the shoaling region under these wave energy conditions.

The high spatial resolution of the laser–video system allowed detailed observation of ripple shape. The mean transition ripple wavelength was 8.5 ± 0.5 cm and height was 0.3 ± 0.1 cm. During offshore migration the ripple profiles were slightly positively skewed and pitched forward in the direction of migration. In terms of the ripple wavelength–orbital diameter based classification proposed by *Clifton and Dingler* [1984], these observations indicate that the anorbital ripple class extends farther into a smaller orbital diameter range than suggested by the schematic diagram (Figure 10).

The ripple migration rate was well correlated with the skewness and third moment of the wave orbital velocity ($r^2 > 0.7$). Both onshore and offshore ripple migration were observed, with average rates of −0.4 cm/min offshore and 0.2 cm/min onshore. The average orbital velocity skewness was −0.17 (0.16) during offshore (onshore) ripple migration, and skewness and migration velocity were correlated for both cross-shore directions. A weak offshore mean flow velocity (−3 cm/s average) resulted in a small negative offset in ripple migration velocity. As far as the authors are aware, these observations provide the first evidence of both onshore and offshore skewness-related ripple migration.

During storm growth the wave power spectral density was bimodal, and the bispectrum indicated a difference interaction between the sea and swell frequency waves, producing negative orbital velocity skewness. In contrast, during storm decay the orbital velocity had a single swell frequency spectral peak, and the bispectrum showed positive skewness arising through self-self interaction of the residual swell. The average negative orbital velocity skewness predicted by a finite depth second-order wave interaction theory based on the two-frequency equations of *Biésel* [1952] was −0.10, roughly consistent with the observations. A more complete wave description is required to model the observed positive velocity skewness, which was overpredicted at 0.6. The range of validity of the second-order theory was exceeded in this case, as indicated by Ursell numbers > 0.3. Work is underway on comparison with the more general *Hasselman et al.* [1963] second-order theory which uses the full velocity spectrum.

These observations of the small-scale directional response of the seabed during a single storm event on an unbarred pocket beach have implications for larger scale beach morphology change. In a typical beach storm cycle, sediment is removed from the beach during the initial stages of a storm and replaced during the calm conditions that follow [*Komar*, 1998, chap. 7]. The results presented here indicate that as the storm grew in intensity, locally generated wind waves interacted with swell to produce negative velocity skewness through sea–swell difference interactions, driving ripples offshore. In contrast, during storm decay the unimodal residual swell led to positive skewness through sum interactions, driving ripples onshore. This wave forcing pattern (sea and swell during storm growth, followed by residual swell after the storm) may be characteristic of many storm events. The ripple migration measurements presented here are consistent with offshore–onshore transport of sand during a beach cycle. Thus these results support nonlinear wave–wave interactions, mediated by wave orbital velocity skewness, as a mechanism for cyclic beach adjustment during storms.

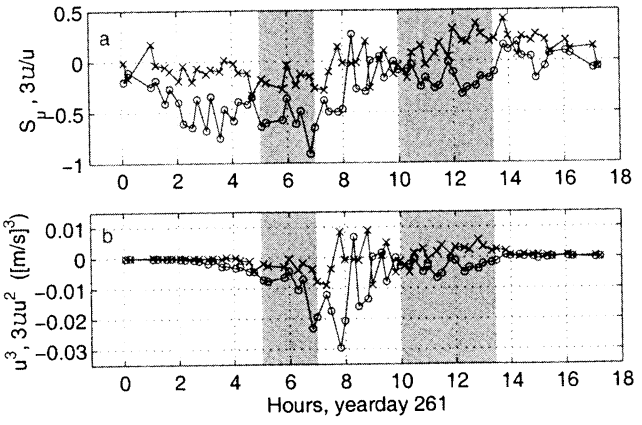

Figure A1. The contribution of the mean velocity $\mathcal{U}$ to u^3_{total}, the term $3\mathcal{U}u^2$. The time series of this term is shown in Figure A1a normalized by $\langle u^2 \rangle^{3/2}$ (line with circles) for comparison with S_u (line with crosses) and in Figure A1b $3\mathcal{U}u^2$ (line with circles) is compared to u^3 (line with crosses). The time periods intervals I and II are shaded gray.

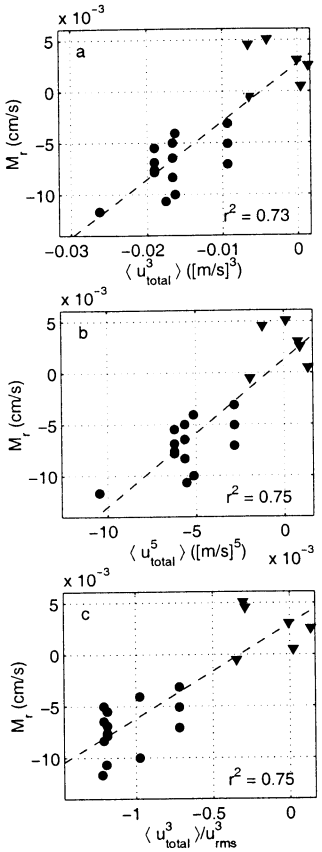

Figure A2. Regressions of ripple migration velocity and several odd power total velocity quantities: (a) total velocity cubed, (b) total velocity to the fifth power, and (c) total velocity cubed, normalized by u_{rms} cubed. Measurements during interval I are shown by circles and those during interval II are shown by triangles.

Appendix A: Mean Velocity Contributions

The preceding analysis centered on the nearbed velocity measured by the CDP, which was demeaned to

determine the orbital velocity, that part of the total nearbed velocity due to the waves directly. If the total velocity, $u_{\text{total}} = \mathcal{U} + u$, is considered, the effect of the mean velocity $\mathcal{U}$ on quantities based on the time average of velocity cubed can be assessed by examining the cross term $3\mathcal{U}u^2$. Figure A1 illustrates this quantity compared with u^3, and also normalized by $\langle u^2 \rangle^{3/2}$ compared with the skewness of u.

The sense of the mean velocity cross term contribution to u^3_{total} during both intervals I and II is negative, or offshore, even during the time when ripples were migrating onshore in interval II. The dynamical significance of this term may be in the negative offset in ripple migration velocity seen in the regression in Figure 12. Including the mean velocity, i.e., regressing to u^3_{total}, does not affect the correlation coefficient but removes the critical directional dependence, as shown in Figure A2a. Regressions to u^5_{total} and $u^3_{\text{total}}/u^3_{\text{rms}}$ are also shown in Figure A2. These show similarly strong correlations with the ripple migration velocity and do not themselves support the choice of one velocity exponent over the other.

Notation

a_o wave orbital semiexcursion.
A asymmetry.
A_b predicted percentage of waves breaking.
$\mathcal{A}_i$ second-order u fundamental coefficient.
B bispectrum.
$\mathcal{B}_i$ second order u harmonic coefficient.
c wave phase speed.
C complex Fourier coefficient.
D_{16} sixteenth percentile grain diameter.
D_{50} median grain diameter.
D_{84} 84th percentile grain diameter.
$\mathcal{D}_{21}$ second-order u difference frequency coefficient.
$E\{\ \}$ expectation value.
f frequency.
f_w wave friction factor.
g acceleration due to gravity.
h water depth.
$H_{1/3}$ significant wave height.
H_b wave breaking height.
H_o deep water significant wave height.
L_o deep water wavelength.
M_r ripple migration velocity.
r^2 correlation coefficient.
$\Re\{\ \}$ real part.
s specific gravity.
S skewness.
$\mathcal{S}_{21}$ second-order u sum frequency coefficient.
t time.
T_p wave orbital velocity spectrum peak period.
T_ζ surface elevation spectrum peak period.
u nearbed orbital velocity (demeaned).
u_s nearbed streaming velocity.
Ur Ursell number.
$\mathcal{U}$ mean nearbed velocity.
u_{total} total nearbed velocity.
β bicoherence.
γ breaking wave height coefficient.
λ_r ripple wavelength.
η_r ripple height.
$\theta_{2.5}$ grain roughness Shields parameter.
ω radian frequency.
ζ sea surface elevation.

Acknowledgments. This work was funded by the Natural Science and Engineering Research Council of Canada and the U.S. Office of Naval Research Coastal Sciences Program. The authors thank Steve Elgar and Steve Henderson for useful discussion on bispectral analysis, Bob Guza for helpful comments on nonlinear wave theory, and members of the departments at both universities involved in the field work.

References

Allen, J. R. L., A model for the interpretation of wave ripple-marks using their wavelength, textural composition, and shape, *J. Geol. Soc. London*, *136*, 673–682, 1979.

Bagnold, R. A., Beach and nearshore processes, in *The Sea, vol. 3*, edited by M. N. Hill, pp. 507–553, Wiley-Interscience, New York, 1963.

Bailard, J. A., and D. L. Inman, An energetics bedload model for a plane sloping beach: Local transport, *J. Geophys. Res.*, *86*, 2035–2043, 1981.

Biésel, F., Équations générals au second ordre de la houle irrégulaire, *Houille Blanche*, *3*, 372–376, 1952.

Clifton, H. E., Wave-formed sedimentary structures—A conceptual model, in *Beach and Nearshore Sedimentation*, edited by R. A. Davis Jr and R. L. Ethington, *Spec. Publ. SEPM Soc. Sediment. Geol.*, *24*, 126–148, 1976.

Clifton, H. E., and J. R. Dingler, Wave-formed structures and paleoenvironmental reconstruction, *Mar. Geol.*, *60*, 165–198, 1984.

Conley, D. C., and D. L. Inman, Field observations of the fluid-granular boundary layer under near-breaking waves, *J. Geophys. Res.*, *97*, 9631–9643, 1992.

Crawford, A. M., Field observations of ripple migration and orbital velocity skewness, Ph.D. thesis, Mem. Univ. of Newfoundland, St. John's, Newfoundland, Canada, 2000.

Crawford, A. M., and A. E. Hay, A simple system for laser-illuminated video imaging of sediment suspension and bed topography, *IEEE J. Oceanic Eng.*, *23*, 12–19, 1998.

Dingler, J. R., Wave formed ripples in nearshore sands, Ph.D. thesis, Univ. California, San Diego, 1974.

Dingler, J. R., and D. L. Inman, Wave-formed ripples in nearshore sands, in *Proceedings of the 15th Coastal Engineering Conference, vol. 2*, pp. 2109–2126, Am. Soc. of Civ. Eng., New York, 1977.

Doering, J. C., and A. J. Bowen, Parameterization of orbital velocity asymmetries of shoaling and breaking waves using bispectral analysis, *Coastal Eng.*, *26*, 15–33, 1995.

Dyer, K. R., and R. L. Soulsby, Sand transport on the continental shelf, *Annu. Rev. Fluid Mech.*, *20*, 295–324, 1988.

Elgar, S., and R. T. Guza, Observations of bispectra of shoaling surface gravity waves, *J. Fluid Mech.*, *161*, 425–448, 1985a.

Elgar, S., and R. T. Guza, Shoaling gravity waves: Comparisons between field observations, linear theory, and a nonlinear model, *J. Fluid Mech.*, *158*, 47–70, 1985b.

Elgar, S., and R. T. Guza, Statistics of bicoherence, *IEEE*

Trans. Acoust. Speech Signal Process., *36*, 1667–1668, 1988.

Elgar, S., T. H. C. Herbers, V. Chandran, and R. T. Guza, Higher-order spectral analysis of nonlinear ocean surface gravity waves, *J. Geophys. Res.*, *100*, 4977–4985, 1995.

Guza, R. T., and E. B. Thornton, Local and shoaled comparisons of sea surface elevations, pressures and velocities, *J. Geophys. Res.*, *85*, 1524–1530, 1980.

Hasselman, K., W. Munk, and G. MacDonald, Bispectra of ocean waves, in *Time Series Analysis*, edited by M. Rosenblatt, pp. 125–139, John Wiley, New York, 1963.

Hay, A. E., and A. J. Bowen, Alongshore migration of lunate megaripples during DUCK94: Part 1, *J. Geophys. Res.*, in press, 2001.

Hay, A. E., and D. J. Wilson, Rotary sidescan images of nearshore bedform evolution during a storm, *Mar. Geol.*, *119*, 57–65, 1994.

Hay, A. E., C. Smyth, L. Zedel, and T. Mudge, On remotely probing the structure of the bottom boundary layer over an evolving seabed, in *Coastal Ocean Processes Symposium: A Tribute to William D. Grant, WHOI-99-04*, pp. 99–106, Woods Hole Oceanogr. Inst., Woods Hole, Mass., 1999.

Herbers, T. H. C., and M. C. Burton, Nonlinear shoaling of directionally spread waves on a beach, *J. Geophys. Res.*, *102*, 21,101–21,114, 1997.

Herbers, T. H. C., and R. T. Guza, Nonlinear wave interactions and high-frequency seafloor pressure, *J. Geophys. Res.*, *99*, 10,035–10,048, 1994.

Herbers, T. H. C., R. L. Lowe, and R. T. Guza, Field observations of orbital velocities and pressure in weakly nonlinear surface gravity waves, *J. Fluid Mech.*, *245*, 413–435, 1992.

Kim, Y. C., and E. J. Powers, Digital bispectral analysis and its applications to nonlinear wave interactions, *IEEE Trans. Plasma Sci.*, *7*, 120–131, 1979.

Komar, P. D., *Beach Processes and Sedimentation*, Prentice-Hall, Old Tappan, N. J., 1998.

Kraus, N. C., and K. Horikawa, Nearshore sediment transport, in *The Sea*, edited by B. Le Méhauté and D. M. Hanes, vol. 9, part B, pp. 775–813, John Wiley, New York, 1990.

Lippmann, T. C., E. B. Thornton, and A. J. H. M. Reniers, Wave stress and longshore current on barred profiles, in *Proceedings of Coastal Dynamics '95*, pp. 401–412, Am. Soc. of Civ. Eng., New York, 1996.

Longuet-Higgins, M. S., The mechanics of the boundary-layer near the bottom in a progressive wave, in *Proceedings of the 6th International Conference on Coastal Engineering*, pp. 184–193, Am. Soc. of Civ. Eng., New York, 1957.

Meyer-Peter, E., and R. Müller, Formulas for bed-load transport, in *Report on the 2nd Meeting of the International Association for Hydraulic Structures Research*, vol. 2, pp. 39–64, Int. Assoc. for Hydraul. Struct. Res., Stockholm, 1948.

Miche, M., Movements ondulatoires de la mer en profondeur constante ou decroissante, *Ann. Ponts Chaussées*, *114*, 25–406, 1944.

Nielsen, P., Dynamics and geometry of wave-generated ripples, *J. Geophys. Res.*, *86*, 6467–6472, 1981.

Nielsen, P., *Coastal Bottom Boundary Layers and Sediment Transport*, Adv. Ser. on Ocean Eng., vol. 4, World Sci., Singapore, 1992.

Norheim, C. A., T. H. C. Herbers, and S. Elgar, Nonlinear evolution of surface wave spectra on a beach, *J. Phys. Oceanogr.*, *28*, 1534–1551, 1998.

Phillips, O. M., On the dynamics of unsteady gravity waves of finite amplitude, part 1, The elementary interactions, *J. Fluid Mech.*, *9*, 193–217, 1960.

Sleath, J. F. A., On rolling-grain ripples, *J. Hydraul. Res.*, *14*, 69–81, 1976.

Sleath, J. F. A., Sediment transport by waves and currents, *J. Geophys. Res.*, *100*, 10,977–10,986, 1995.

Thornton, E., and R. T. Guza, Transformation of wave height distribution, *J. Geophys. Res.*, *88*, 5925–5938, 1983.

Thornton, E. B., and R. T. Guza, Wind wave transformation, in *Nearshore Sediment Transport*, edited by R. J. Seymour, pp. 137–171, Plenum, New York, 1989.

Traykovski, P., A. E. Hay, J. D. Irish, and J. F. Lynch, Geometry, migration, and evolution of wave orbital ripples at LEO-15, *J. Geophys. Res.*, *104*, 1505–1524, 1999.

Vincent, C. E., D. M. Hanes, and A. J. Bowen, Acoustic measurements of suspended sand on the shoreface and the control of concentration by bed roughness, *Mar. Geol.*, *96*, 1–18, 1991.

Wiberg, P. L., and C. K. Harris, Ripple geometry in wave-dominated environments, *J. Geophys. Res.*, *99*, 775–789, 1994.

Wilson, D. J., and A. E. Hay, High resolution sidescan sonar observations of small scale sand bedforms under waves: A comparison of field and laboratory measurements, paper presented at the 1995 Canadian Coastal Conference, Natl. Res. Counc., Dartmouth, Nova Scotia, Canada, 1995.

Zedel, L., and A. E. Hay, Direct observations of wave induced sediment flux and turbulent velocities in a wave flume, in *Proceedings of the 26th Conference on Coastal Engineering*, pp. 2607–2614, Am. Soc. of Civ. Eng., New York, 1998.

A. M. Crawford, Defence Research Establishment Atlantic, P. O. Box 1012, Dartmouth, Nova Scotia, Canada, B2Y 3Z7. (Anna.Crawford@drea.dnd.ca)

A. E. Hay, Dalhousie University, Department of Oceanography, Halifax, Nova Scotia, Canada, B3H 4J1. (Alex.Hay@Dal.Ca)

(Received August 25, 2000; revised January 29, 2001; accepted February 16, 2001.)